Comparison of Near- and Far-Field Supercell Inflow Environments Using Radiosonde Observations

ANDREW R. WADE[a]

Cooperative Institute for Mesoscale Meteorological Studies, University of Oklahoma, and NOAA/OAR/National Severe Storms Laboratory, Norman, Oklahoma

MICHAEL C. CONIGLIO AND CONRAD L. ZIEGLER

NOAA/OAR/National Severe Storms Laboratory, Norman, Oklahoma

ABSTRACT

A great deal of research focuses on how the mesoscale environment influences convective storms, but relatively little is known about how supercells modify the nearby environment. Soundings from three field experiments are used to investigate differences in the near and far inflow of supercell thunderstorms. Close-range soundings in the near inflow of supercells are compared to near-simultaneous soundings released farther away (but still within inflow). Several soundings from the second field phase of the Verification of the Origins of Rotation in Tornadoes Experiment (VORTEX2) supplement the Mesoscale Predictability Experiment (MPEX/MiniMPEX) dataset, resulting in 28 near–far inflow pairs from a wide variety of tornadic and nontornadic supercells. The focus of this study is on a comparison of a subset of 12 near–far inflow pairs taken near tornadic supercells and 16 near–far inflow pairs taken near nontornadic supercells. Similar values of 0–1-km storm-relative helicity (SRH01) are found in the far field of the tornadic and nontornadic supercells, possibly as a result of a difference in mean diurnal timing. However, SRH01 is found to increase substantially in the near field of the tornadic supercells, but not the nontornadic supercells. Differences in the thermodynamic environment include greater moisture above the ground in the far field of the tornadic supercells (despite similar near-ground moisture in both the tornadic and nontornadic subsets) and a subtle increase in static stability near the surface in the nontornadic near inflow.

1. Introduction

The importance of the ambient state of the atmosphere to the intensity and organization of deep convection has been thoroughly studied for decades. Early analyses connected vertical wind shear and low-level moisture with tornadoes and hailstorms (Beebe 1956; Whiting and Bailey 1957; Dessens 1960; Williams 1976). More recently, numerous observational studies (e.g., Hart and Korotky 1991; Rasmussen and Blanchard 1998; Thompson et al. 2002; Markowski et al. 2003; Rasmussen 2003; Thompson et al. 2003; Craven and Brooks 2004) have identified relevant quantitative parameters (and combinations thereof) for supercells: convective available potential energy (CAPE),

vertical shear, and storm-relative helicity (SRH) in the lower troposphere, with lifted condensation level (LCL) heights and SRH01 also significant if considering tornado production. Numerical simulations have further established the role of the near-storm environment in modulating convection and accompanying hazards. Prominent examples include exploration of varying buoyancy and shear profiles by Weisman and Klemp (1982), Weisman and Klemp (1984), McCaul and Weisman (2001), Markowski and Richardson (2014), and Coffer and Parker (2017), among others.

Yet the extensive research on supercell and tornado environments has mostly been devoted to the environment's effects on the storm. Comparatively little has been published concerning the reverse: the effect of storms on their environments. Fankhauser (1971) and Barnes (1978) described flow perturbations around mature supercells, and Lilly (1986) composed a kinetic energy cycle for supercells that accounted for energy transfer from the storm

[a] Current affiliation: North Carolina State University, Raleigh, North Carolina.

Corresponding author: Andrew R. Wade, arwade@ncsu.edu

to the mean flow. More recently, Markowski et al. (1998a) and Brooks et al. (1994) noted possible wind profile modification near a passing supercell. Markowski et al. (1998b) and Nowotarski and Markowski (2016) demonstrated effects of low-level cooling from anvil shading in simulated supercells, and the "Goldilocks zone" of Potvin et al. (2010) suggested that environmental profiles within 40 km of ongoing storms are frequently contaminated. In the most comprehensive such work to date, Parker (2014, hereafter P14) produced a composite of supercell near-storm environments using VORTEX2 balloon-borne radiosondes (hereafter referred to as soundings for brevity). There was evidence of 0.5–1.0-K cooling in near-storm inflow caused by cloud shading and/or adiabatic lifting, as well as substantial storm-induced enlargement of nontornadic near-inflow hodographs. The apparent tendency of nontornadic supercells to enlarge hodographs was speculatively attributed to baroclinic effects on the low-level shear vector arising from evaporative cooling in relatively dry low levels. Kerr et al. (2017) demonstrated effects similar to P14's in convection-allowing ensemble analyses of storms.

In view of the well-established influence of the near-storm environment on storm behavior, such alterations to the thermodynamic and kinematic characteristics of inflow could feasibly influence storm structure, intensity, longevity, and/or severe weather production. On the whole, the quantitative nature of inflow modification very near low-level mesocyclones remains unclear. Using in situ observations from three field projects, this work addresses that question with the eventual aim of better understanding supercell behavior, including tornadogenesis and its failure.

2. Data and methods

a. Field campaigns

VORTEX2 (Wurman et al. 2012) remains the most expansive field campaign to target tornado-producing storms. The project's exploration of tornadogenesis and its relationship to the near-storm environment yielded numerous inflow observations from four mobile sounding units. Many of the soundings were located close enough to supercells to reveal any storm-induced modifications to the inflow environment, offering a starting point for this dataset.

One goal of the Mesoscale Predictability Experiment (MPEX) campaign was to investigate the upscale effects of deep convection and the possibility of improving short-term predictability of deep convection with targeted mesoscale observations (Weisman et al. 2015; Trapp et al. 2016). The field phase was conducted in spring 2013 with contributions from mobile sounding vehicles from the National Severe Storms Laboratory (NSSL), Colorado State University (CSU), Purdue University (PU), and Texas A&M University (TAMU). All units used Inter-Met radiosonde systems except for CSU, which used Vaisala systems. Details of MPEX upsonde operations may be found in Trapp et al. (2016). MPEX contributed 54 supercell inflow soundings to this dataset (criteria used to define inflow soundings are given in section 2c).

In spring of 2016 a small field project (termed MiniMPEX) was conducted with two NSSL mobile sounding vehicles to add substantially to the dataset of supercell inflow soundings obtained from MPEX. Whereas all sides of storms were sampled in MPEX (Trapp et al. 2016), MiniMPEX focused on releasing radiosondes into the inflow of supercells, sampling both the near-field and far-field inflow, simultaneously when possible. A total of 52 supercell inflow soundings over 10 days were obtained in MiniMPEX, resulting in a combined MPEX/MiniMPEX dataset containing 106 supercell inflow soundings.

b. Data quality control

Sounding data from VORTEX2 and MPEX were quality controlled mostly by the National Center for Atmospheric Research/Earth Observing Laboratory (NCAR/EOL; Loehrer et al. 1998). However, data obtained in MiniMPEX were quality controlled by the authors. Following the general procedures of Loehrer et al. (1998), the raw 1-Hz data from the MiniMPEX soundings were plotted and manually examined for obvious errors in temperature, humidity, pressure, and wind. Any data point with a higher pressure than the previous valid data point was removed, eliminating both vertical oscillations due to storm-scale downdrafts and the rapid descent of the sonde after balloon rupture. Some levels had valid data for certain variables and invalid/missing data for others; in such cases, interpolation (linear on a $\log p$ scale) was used to complete the profile.

Each sounding vehicle during MiniMPEX was equipped with a mobile mesonet unit (e.g., Straka et al. 1996) recording atmospheric pressure, temperature, relative humidity, and wind speed and direction at 1-s intervals. As a final quality-control step, temperature, humidity, and wind data obtained from mobile mesonet (MM) instruments mounted on the top of the vehicles were inserted as the lowest level of each MiniMPEX sounding, as was done for the VORTEX2 and MPEX soundings. By prescribing the surface wind value and considering the profile filter effects described below, the winds both surface and aloft within the surface layer during the first several seconds after launch were effectively replaced by the surface MM-measured value to correct for the effects of the balloon acceleration from rest after launch in shear (Yurchak 2013). Because sounding crews took care to

minimize exposure errors, mean differences between raw radiosonde data just above the surface and MM observations were found to be small.

Care must be taken to mitigate the effects of "pendulum oscillation" of the radiosonde beneath the balloon, which appears with a semiregular period of 10–20 s in raw GPS-derived wind data. Filtering of the wind data by cubic splines, a moving average, and a weighted average using a triangular filter was tested. All methods produced similar results, but some differences on the order of the instrument error were found near the ground (and at the top of the profile) where the data must be extrapolated to maintain an equal number of data points used in the averaging filters. A cubic spline is found to yield the most acceptable results (and those most similar to the EOL quality-controlled soundings above the surface layer), likely because this method fits a third-order polynomial piecewise to the data near the ground with no truncation/extrapolation of the data series required. The one-dimensional approximating cubic spline algorithm implemented in the NCAR command language (UCAR/NCAR/CISL/TDD 2014) is used with "knots" (points) every 200 m in the vertical. An example of this cubic spline applied to a raw radiosonde wind field from MiniMPEX is shown in Fig. 1.

For determining SRH, observed storm motion was desired, both for accuracy and because soundings often did not reach the 6 km AGL required for calculating Bunkers's supercell motion (Bunkers et al. 2000). The center of the mesocyclone was manually located using the nearest WSR-88D at the lowest tilt of the scan nearest to launch time. It was located again 1 hour later. The range and bearing from the first to the second were used to define the observed storm motion over the hour following launch. This motion was calculated for each sounding individually.

c. Near–far inflow pair selection

In total, MPEX and MiniMPEX obtained 106 supercell inflow soundings. Ideally, each would be compared to some base state or background environment entirely uninfluenced by the storm. In the appendix it is shown that RAP analysis "soundings" are unsuitable for use as these background profiles. This necessitates restricting the dataset to near-simultaneous pairs of observed soundings: one in the near inflow of a supercell and one in the inflow farther away. To constitute a valid near–far pair, the distant sounding must have been launched at least 10 km farther afield than the near sounding, and the two must have been released within 30 min of each other. This usually resulted in the far-field half of the pair being more than 40 km from the storm. A distance of 40 km or more is desirable for an uncontaminated
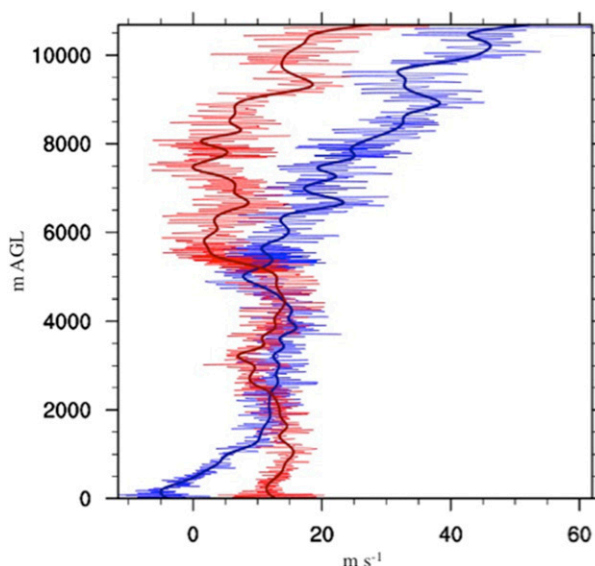

FIG. 1. An example of the filtered zonal (thick blue line) and meridional (thick red line) wind components (m s^{-1} on the abscissa) vs height (m AGL on the ordinate) obtained by the approximating cubic spline applied to the raw GPS-derived wind data (thin lines) for a sounding released 2047 UTC 9 May 2016.

"proximity" sounding since Potvin et al. (2010) conclude that the likelihood of soundings being contaminated by the storm decreases rapidly as they are taken more than 40 km from an ongoing storm. Care was taken to ensure that sounding pairs that appeared to sample different mesoscale or larger air masses were excluded.

These criteria produced a set of 20 near–far pairs from MPEX and MiniMPEX. These pairs were supplemented with 8 pairs from VORTEX2 for a total of 28 near–far pairs (Table 1). There were 12 pairs designated as "tornadic," from supercells that were producing tornadoes at the near-field sounding release time or did so within an hour after release. The 16 pairs not meeting that criterion were designated "nontornadic." It would be preferable to compare only nontornadic and significantly (EF2+) tornadic storms. However, suitable sounding pairs near significant tornadoes are understandably scarce and such a comparison would require much more data collection. The 12 tornadic pairs were sampled from 9 tornadic supercells, and the 16 nontornadic pairs were sampled from 10 nontornadic supercells. Four supercells were sampled as both tornadic and nontornadic in different phases of their evolution. Two of the nontornadic pairs and six of the tornadic pairs were taken from events included in P14's composite supercell environments. Occasional use of multiple pairs from a single storm might arguably constitute oversampling, but the hour or more required to complete a sounding and prepare another enforces at least some

TABLE 1. All pairs of inflow soundings used in near- and far-field statistics and composites.

Date	Time (UTC)	Location	Tornadic
5 Jun 2009	2143	W NE-SE WY	Y
18 May 2010	2152–2159	TX Panhandle	Y
18 May 2010	2255–2257	TX Panhandle	Y
19 May 2010	2059–2100	NW OK	N
19 May 2010	2257–2259	Central OK	Y
25 May 2010	2326–2327	W KS	Y
26 May 2010	0030–0033	W KS	N
8 Jun 2010	0035–0040	W NE	Y
23 May 2013	1928–1947	NW TX	Y
28 May 2013	0035–0055	Central KS	N
26 Apr 2016	2155–2204	SW OK	N
26 Apr 2016	2252–2256	SW OK	N
26 Apr 2016	2347–2351	Central OK	N
29 Apr 2016	1934–1935	SW OK	Y
29 Apr 2016	2042–2044	SW OK	Y
29 Apr 2016	2141–2146	Central OK	N
9 May 2016	2046–2052	S OK	Y
16 May 2016	2253–2256	TX Panhandle	N
16 May 2016	2351–2353	TX Panhandle	N
17 May 2016	0050–0100	TX Panhandle	Y
23 May 2016	2131–2146	TX Panhandle	N
26 May 2016	0256	N OK	Y
26 May 2016	0334–0345	N OK	N
26 May 2016	2312–2320	S KS	N
27 May 2016	0027–0036	S KS	N
27 May 2016	2232–2306	S OK	N
27 May 2016	2332–2335	S OK	N
28 May 2016	0040–0117	S OK	N

FIG. 2. Line segments connecting the storm-relative release points of the 28 approximately simultaneous near–far sounding pairs. Dotted black and magenta lines denote mean VORTEX2 and MPEX/MiniMPEX sounding pair locations. The radar-estimated center of the low-level mesocyclone is at the origin. Observed mesocyclone motion is along the positive x axis.

amount of independence. P14 used many more soundings from fewer storm days. Although the sample sizes limit our ability to generalize behavior from the statistical properties of the dataset, they represent a modest improvement on the number of supercells sampled for the P14 composites. Since observed soundings within 40 km of tornadic supercells with simultaneous far-field soundings for comparison do not occur unless specifically sought in field research, this is the largest such dataset that currently exists to the authors' knowledge. Still, future work in this area would greatly benefit from further mobile sounding operations in the mold of MiniMPEX.

Several additional notes on the dataset are in order. First, the sampling strategies for distant inflow soundings differed from VORTEX2 to MPEX/MiniMPEX. VORTEX2 soundings were often released close to the eventual path of the storm's updraft, while MPEX/MiniMPEX far-field soundings were typically released farther to the right of the storm's path. The difference is noted in Fig. 2, which shows the storm-relative location of each pair. Second, there is no meaningful difference between the ranges of tornadic and nontornadic near-field soundings (means of 26 and 25 km from the storm, respectively). Differences between tornadic and nontornadic near-field
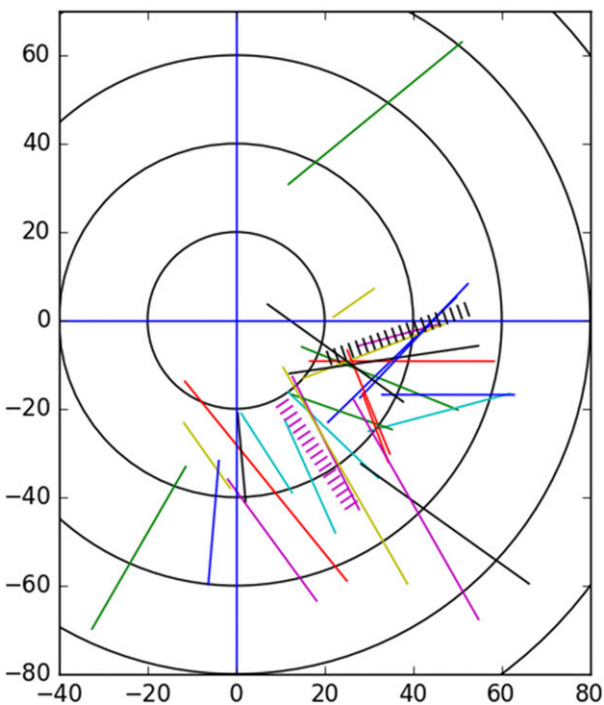
environments noted later are not due to differences in the distances of the soundings to the storms. The same is true for the far-field soundings. Third, the tornadic sounding pairs as a group occurred earlier in the day than the non-tornadic pairs (Fig. 3a) and at higher elevation (Fig. 3b). This is an example of how such work would benefit from a larger sample, since effects of diurnal timing and surface elevation may obfuscate results. Impacts of these discrepancies are discussed in the following sections. Fourth, the mean near-field range (26 km from the storm) and far-field range (56 km) are both nearer than the points selected to represent the near and far inflow in P14's objective analyses: 40 and 80 km from the storm. Finally, the fundamental assumption required for comparing simultaneous near- and far-field soundings is that the two soundings would be roughly identical in the absence of the supercell—that is, that there are no significant mesoscale heterogeneities in the sampled environment. This assumption is never perfectly fulfilled in an attempt to observe near-storm, storm-induced phenomena, as the true state of the atmosphere absent the storm cannot be known. Furthermore, little is known about the ambient spatiotemporal variability of the relevant parameters on the scale in question. Markowski et al. (1998a) documented variability of SRH in VORTEX
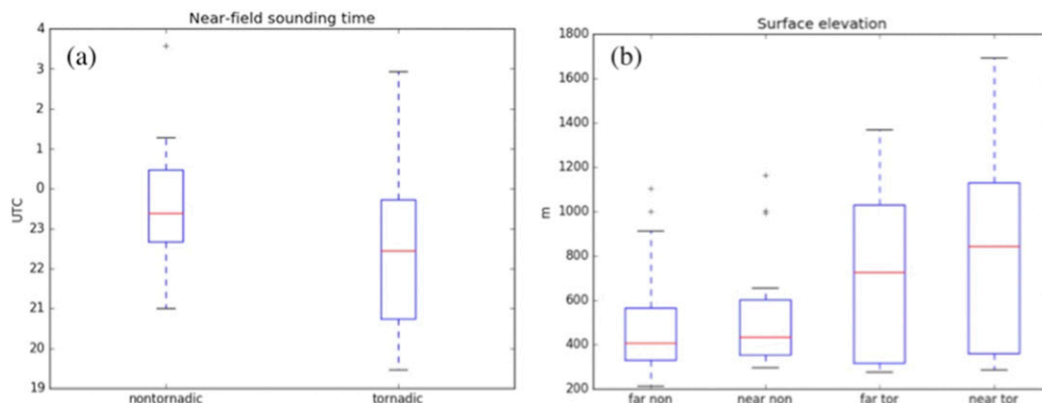
FIG. 3. Boxplots of (a) near-field sounding release time and (b) elevation above mean sea level of sounding release points. Here and in following boxplots, red lines represent the median, boxes display the interquartile range, and whiskers extend to the most extreme values within 1.5 times the interquartile range, with more extreme values plotted as single points.

cases, but on scales of ~100 km and usually in the presence of well-defined boundaries. Sounding pairs in this study averaged 30 km apart and were never separated by any evident boundary.

3. Results and discussion

a. Near-minus-far perturbations

Results presented here are from an analysis of the 28 pairs of near-simultaneous soundings in the near and far inflow of supercells, rather than the full set of supercell inflow soundings. Values of relevant variables in far-field inflow soundings were subtracted from the corresponding near-field values to yield distributions of near-storm perturbations from the background environment. This section describes those results.

Figure 4a shows distributions of surface temperature perturbations for tornadic sounding pairs and nontornadic pairs. Many pairs cool somewhat in the near field, as in P14, and warming of more than 0.5 K is seldom observed. Both tornadic and nontornadic perturbation distributions are centered near zero. However, the interquartile range of nontornadic pairs extends into larger negative perturbations than that of the tornadic pairs.

Surface temperature perturbations must be treated with caution because of the effect of elevation. Nearly all near-field soundings were released farther west and at slightly higher elevation than the corresponding far-field soundings, such that a hypothetical inflow parcel passing through both points would experience adiabatic cooling independent of the storm. However, elevation is not the only possible cause of the cooler surface temperatures observed in the near inflow. Anvil shading can also produce a shallow, cooler, statically stable layer at the surface (Markowski et al. 1998b; Nowotarski and Markowski 2016).

To remove the effect of upslope adiabatic cooling from the distant inflow to the near inflow, surface potential temperature was calculated for each sounding. Anvil shading, insolation, and any other diabatic effects should appear as changes in potential temperature. The results are shown in Fig. 4b. There is scant evidence of net diabatic cooling in the near field of tornadic storms. For nontornadic storms, although most near-inflow perturbations are small, there is slight cooling on average and a few perturbations reach −2 K. The studies of anvil shading mentioned above focus on areas close to the forward-flank gust front and near the path of the storm, where inflow parcels likely have longer residence times beneath the storm's anvil. While near-inflow soundings during MiniMPEX were nearly always released in the anvil's shadow, it is possible that they sampled near-surface parcels that had not been shaded for very long and remaining insolation canceled the effect of shading, since they tended to be closer to the edge of the shadow to the right of the storm's path (Fig. 2). Although these parcels take different paths than the forward-flank-adjacent inflow parcels examined in previous studies, MPEX and MiniMPEX still lost numerous sondes to updraft ingestion from these more rightward inflow locations.

Figure 4c contains boxplots of changes in surface relative humidity. While distributions for both tornadic and nontornadic subsets appear centered around a slight increase in the near inflow—consistent with the slight cooling and boundary layer moistening in P14—the changes in RH are fairly variable and the mean increase is small. The slight increase is mostly attributable to cooling; dewpoint temperature perturbations (not shown) are small and average near zero for both tornadic and nontornadic cases. Because this is restricted to a shallow layer at
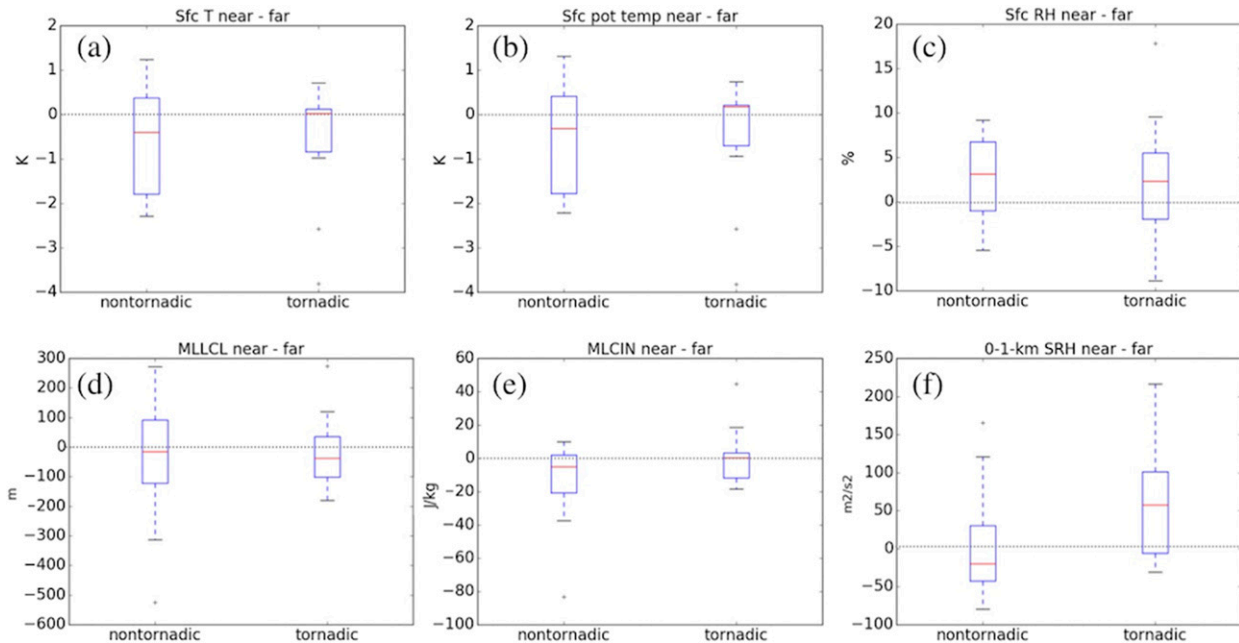
FIG. 4. Distributions of perturbations of relevant parameters for observed sounding pairs. These perturbations are defined as the near-field value minus the far-field (or background) value.

the surface, mixed-layer (lowest 100-hPa average) LCLs (Fig. 4d) change very little in the near inflow for tornadic and nontornadic cases.

P14 reported a modest increase in CIN in the near inflow of the composite supercell environment for both tornadic and nontornadic cases. Likewise, Nowotarski and Markowski (2016) found that anvil shading decreased buoyancy in the boundary layer in supercell simulations. Figure 4e shows boxplots of 100-hPa MLCIN perturbations. (CIN is treated as positive for these distributions, so a positive value means there was more CIN in the near inflow than in the far inflow.) These pairs failed to find any consistent increase in MLCIN in the near inflow. MLCIN seldom changed by more than $20\,\mathrm{J\,kg^{-1}}$ in either direction. Furthermore, although the focus of this study is on the changes to the environment in the near inflow, a noteworthy (if unsurprising) finding is that MLCIN tends to be smaller in the tornadic far-field environment. Nearly 75% of the tornadic far-field soundings have MLCIN $< 20\,\mathrm{J\,kg^{-1}}$, whereas most of the nontornadic far-field soundings have MLCIN $> 20\,\mathrm{J\,kg^{-1}}$. This result is a testament to the importance of including convective inhibition in the significant tornado parameter (Thompson et al. 2012).

The most consistent and robust finding in examining distributions of near-field perturbations is the enlargement of low-level hodographs by tornadic supercells. Figure 4f shows SRH01 perturbations from the far inflow to the near inflow. There is a distinct difference

between tornadic and nontornadic cases: only in the near inflow of tornadic supercells does SRH01 appear to be consistently enhanced. The difference between mean tornadic and nontornadic perturbations is statistically significant. Despite the small samples and wide distributions, bootstrap testing yielded a p value less than 0.05. (Bootstrap testing on other variables found the differences between mean tornadic and nontornadic perturbations to have p values > 0.05, and/or magnitudes too small to be physically useful.) This result seems to contradict the P14 composite environments, in which nontornadic supercells increased the near-field SRH more than tornadic supercells did. This could be a result of both the near- and far-field soundings in this dataset being, on average, closer to the storm than the near and far inflow points defined in P14. Another key difference is that here, SRH01 is computed from soundings that drifted with the surrounding flow, as opposed to vertical profiles drawn from an objective analysis of sounding data in P14. This generally resulted in the sonde drawing even closer to the low-level updraft after release, and presumably experiencing greater accelerations toward the storm.

b. Composite soundings

To characterize the mean storm-induced modifications to a typical inflow environment, composite soundings were created for the near-field tornadic, far-field tornadic, near-field nontornadic, and far-field nontornadic subsets. These composites only extend from the surface to 3 km
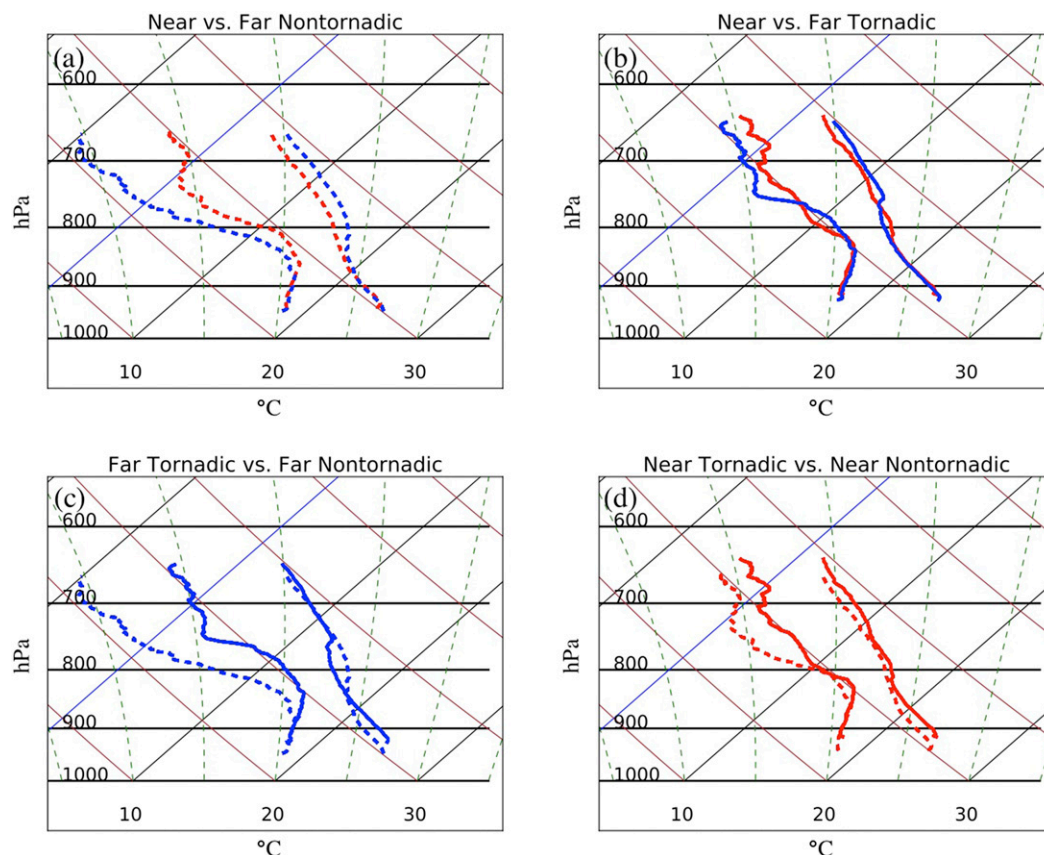
FIG. 5. Skew T–log$p$ diagrams comparing composite soundings for (a) nontornadic (dotted line) near (red line) and far (blue line) inflow, (b) tornadic (solid line) near and far inflow, (c) far tornadic and nontornadic inflow, and (d) near tornadic and nontornadic inflow.

AGL because many soundings ended in midlevels with loss of sonde signal and because of increasing sonde drift with height. For creation of these composites, each observed and quality-controlled sounding was interpolated linearly with respect to height to a 10-m grid in the vertical. All sounding variables (temperature, pressure, dewpoint and relative humidity, and wind components) were then averaged at each level to create the composites.

In comparing near-field and far-field nontornadic soundings (Fig. 5a), two features are noteworthy. First, there is marked cooling and moistening above the boundary layer. Evaporation may be a factor near the top of the composite profiles, since sondes sometimes drifted close to forward-flank precipitation and the far-field profile was often very dry above the boundary layer. However, lifting would also result in similar cooling and moistening. For example, for an ambient lapse rate of $7 \, \mathrm{K \, km^{-1}}$, in the 3000 s required for a $10 \, \mathrm{m \, s^{-1}}$ flow to traverse the mean 30 km between soundings, 1 K of cooling at a fixed altitude is achieved with only $\sim 0.1 \, \mathrm{m \, s^{-1}}$ of dry adiabatic ascent. To further confirm this, the far-field nontornadic composite has been modified using an idealized 1.5-dimensional kinematic model to impose an assumed mesoscale lifting profile following Ziegler and Rasmussen (1998) and Ziegler et al. (2010). After 83 min the result (Fig. 6) is nearly identical to the nontornadic near-field composite. Also, the midtropospheric moistening and cooling evidenced between the far- and near-field tornadic composites (Fig. 5b) may be accomplished via a similar elevated lifting.

Second, a more statically stable layer very near the surface, not so pronounced in the far inflow, appears in the near inflow for the nontornadic soundings. The reason for this very shallow stabilization is not clear. The cooling is not entirely a manifestation of nocturnal cooling, despite the relatively late timing of the nontornadic soundings, because it is more evident in the near-field composite than in the far field. In contrast, the near- and far-field tornadic composite soundings (Fig. 5b) do not show this shallow increase in static stability in the near-field inflow. Ultimately, however, such shallow ($\sim 100 \, \mathrm{m}$) and subtle ($\sim 0.5 \, \mathrm{K}$) features are highly sensitive to any
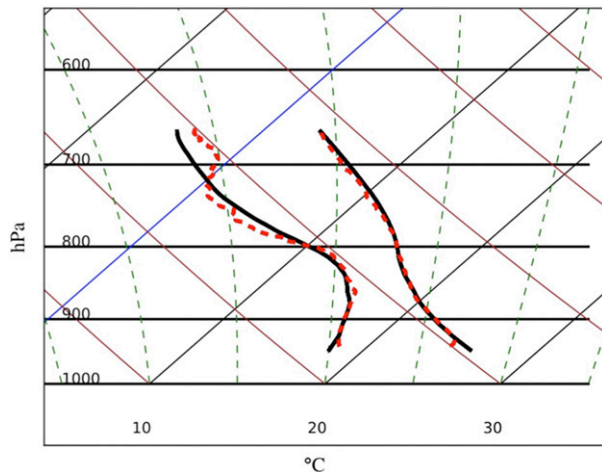
FIG. 6. Near-field nontornadic composite (dotted red) and idealized model output (black) resulting from lifting the far-field nontornadic composite.

exposure error in MM or radiosonde data, and may not affect characteristics of bulk inflow over a mean layer; the MLCIN perturbations do not noticeably reflect them. These results should not be considered as robust as the modifications to the near-storm wind field that will be discussed below.

Elsewhere, the temperature and moisture profiles throughout the 3-km depth of the analysis are more similar in the near- and far-field tornadic environments than the near- and far-field nontornadic composites. This is likely related to lower dewpoint depressions above the boundary layer in the far-field tornadic soundings than in the far-field nontornadic soundings, so there is less potential moistening in the tornadic soundings.

Far-field composites for tornadic and nontornadic supercells are compared in Fig. 5c. This comparison requires some caution because of the discrepancy in diurnal timing mentioned earlier, with tornadic soundings averaging more than an hour earlier in the day than nontornadic ones. The result of a deeper boundary layer with steeper low-level lapse rates in approximately the 900–800-hPa layer in the tornadic composite could be related to this discrepancy in timing between the sounding datasets, as the tornadic soundings tended to be taken closer to peak heating. Even so, the greater depth of moisture and higher humidity in the lowest 3 km in the tornadic soundings is a substantial finding; the deeper/warmer boundary layer closer to the time of peak heating does not result in a much drier boundary layer, as would be expected with similar amounts of background moisture. The low-level tornadic updrafts may experience less dilution from relatively dry air (e.g., James and Markowski 2010) and thus result in stronger

low-level updrafts. Dryness above the boundary layer may further oppose tornado production by inducing low-precipitation supercell structure through midlevel entrainment (Grant and van den Heever 2014) or outflow dominance through enhanced evaporation in downdrafts (Gilmore and Wicker 1998). MiniMPEX observed both of these outcomes on several occasions. Near-field tornadic and nontornadic composite skew T–log$p$ diagrams are overlaid in Fig. 5d. Apart from the subtle and shallow stabilization at the surface, which may be a little stronger in the nontornadic profile, and the overall slightly warmer boundary layer in the tornadic profile, there is little difference between these composites.

Near- and far-field nontornadic hodographs are overlaid in Fig. 7a. They are nearly identical. The mean SRH01 for each of these sets (calculated as the mean of the individual profiles' SRH01 values rather than the SRH01 of the composite profile) is $167 \, m^2 \, s^{-2}$. In contrast to the nontornadic soundings, the composite hodograph for the tornadic soundings is significantly enlarged in the near inflow (Fig. 7b). This demonstrates the increase in SRH01 near tornadic supercells that is seen in the near-field perturbations (Fig. 5f). The mean SRH01 for the far-field tornadic set is $158 \, m^2 \, s^{-2}$, compared to $217 \, m^2 \, s^{-2}$ in the near field. While in some cases the background environment may have larger SRH01 closer to where the storm develops, the short distance (~30 km) between typical near and far soundings suggests that without the presence of any mesoscale boundary (sounding pairs were not used if a boundary was present), these significant differences in SRH01 likely arise from acceleration toward storm-induced negative pressure perturbations. This result appears to contradict P14's finding that nontornadic supercells enhance SRH more than tornadic supercells by enlarging the near-inflow hodograph. The differences in methodology described in the preceding discussion of SRH01 perturbations must be considered here as well. The vertical depth of the hodograph enlargement may be greater than intuitively expected, but Fig. 5 in Houston (2017) depicts idealized mesocyclone-induced radial inflow extending through such a deep layer.

There were a few cases—notably, the 9 May 2016 significantly tornadic supercell near Katie, Oklahoma—in which this effect was not observed. It is hypothesized that substantial enhancement of the low-level wind field is confined to a relatively small sector of the inflow and may require a mature supercell; the Katie storm had only recently become supercellular when the sounding pair used for this study was obtained. In contrast, a briefly tornadic supercell near Fletcher, Oklahoma, on 29 April 2016 was sampled after the storm had matured
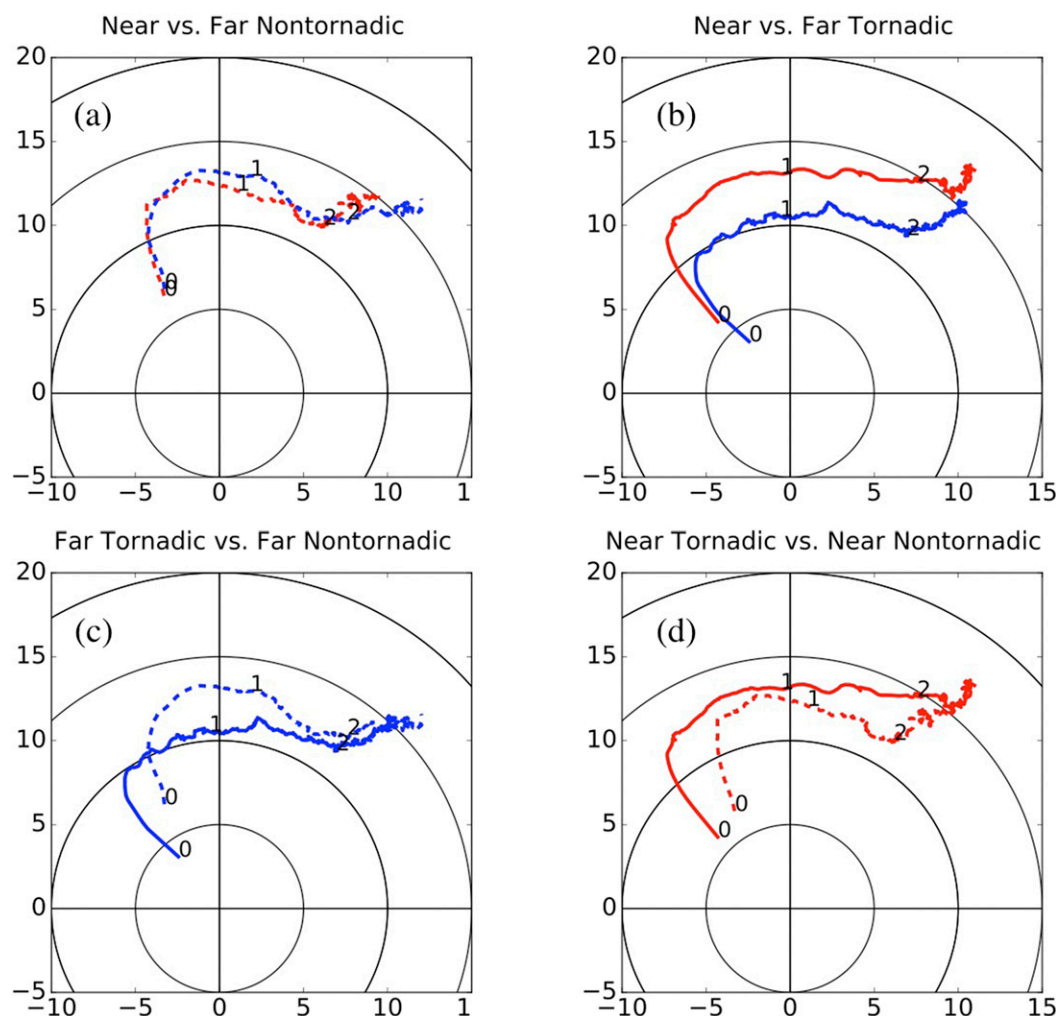
FIG. 7. Hodographs comparing the same composites as in Fig. 5, with the same convention of line style and color. Here and in following hodographs, winds are in m s^{-1} with rings plotted every 5 m s^{-1}. Altitudes of 0, 1, and 2 km AGL are annotated.

for a few hours and showed a large increase in SRH01 in the near field. Figure 8 juxtaposes the 29 April and 9 May 2016 cases for comparison. Still, the small size of the present dataset precludes any serious analysis of the dependence of inflow modification on maturity of the supercell.

Composite far-field hodographs between the tornadic and nontornadic soundings (Fig. 7c) look similar except for the stronger southerly wind component in the nontornadic profile. This may represent the incipient low-level jet in the early evening—although the fact that it exists at all levels below 3 km (not just at the typical low-level jet level of ~250–750 m) suggest stronger *background* southerly winds are present in the nontornadic soundings. Hodograph sizes do not differ significantly in the far field of the tornadic and nontornadic soundings,

but the tornadic hodograph is somewhat "sickle" shaped (i.e., having a sharp kink in the hodograph in the lowest 1 km), as seen in many tornadic environments (Wicker 1996; Thompson and Edwards 2000; Miller 2006; Esterheld and Giuliano 2008). However, the shape of the composite tornadic hodograph also resembles the *nontornadic* hodographs in P14 and Coffer and Parker (2017). This does not necessarily challenge the demonstrated roles of streamwise and crosswise low-level vorticity. Rather, it shows that weak tornadoes often occur in spite of considerable crosswise vorticity, in agreement with the ensemble simulations of Coffer et al. (2017).

In the near-field composite hodographs (Fig. 7d), the tornadic hodograph is notably larger than the nontornadic hodograph, with a larger SRH01 now noted for
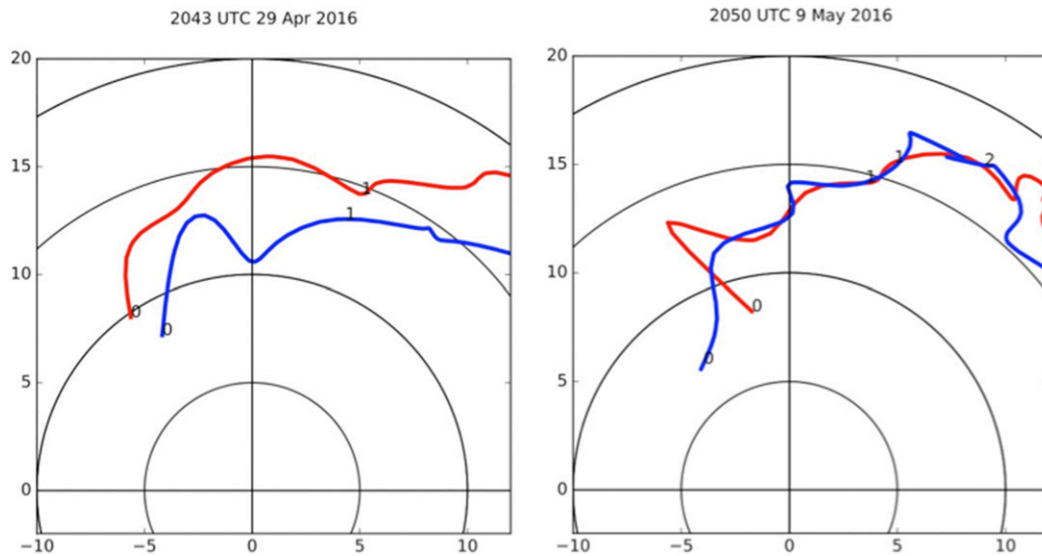
2043 UTC 29 Apr 2016   2050 UTC 9 May 2016

FIG. 8. Near-field (red) and far-field (blue) hodograph comparisons for (left) a mature, briefly tornadic supercell and (right) a young, significantly tornadic supercell.

the tornadic soundings, related to the slightly more backed winds near the ground. However, the subtle difference in hodograph shape between nontornadic and tornadic soundings seen in the far-field composites is less evident in the near-field composites. Both hodographs show a kink near 0.5 km with similar veering from 0.5 to 3 km.

c. El Reno tornado

In light of these results, it should be noted that an outlier was omitted from the analysis. At 2300 UTC 31 May 2013, MPEX crews released a sounding 27 km south-southeast of a supercell just before it produced an intense tornado near El Reno, Oklahoma. The 0000 UTC sounding ~60 km southeast in Norman, Oklahoma, satisfied far-field criteria. Dramatic enlargement of the near-field hodograph is seen in Fig. 9. The storm's infamously erratic motion complicates SRH calculations, but an estimate of $10 \, \mathrm{m \, s^{-1}}$ due eastward yields $244 \, \mathrm{m^2 \, s^{-2}}$ SRH01 for the Norman profile and $704 \, \mathrm{m^2 \, s^{-2}}$ for the El Reno profile. Because of the unusual size of the El Reno hodograph and the record width of the tornado produced, this pair was excluded from the composites and statistical testing as an extreme outlier. However, it remains a compelling example of low-level hodograph enlargement near a tornadic supercell.

4. Summary and conclusions

Observed soundings from VORTEX2, MPEX, and MiniMPEX were used to explore supercell inflow environments and potential differences in how tornadic and nontornadic supercells modify their environments.

To isolate storm-induced changes to the inflow environment, near-storm inflow soundings were compared to near-simultaneously observed profiles farther afield. These pairs of soundings were classified by tornado production. Changes in the near inflow were investigated both as distributions of perturbations in individual soundings and as differences in composite soundings. These findings elucidate the nature of inflow modification by supercells, and provide some context for interpreting observations in the immediate vicinity of ongoing supercells.

The most substantial observed change in the inflow environment from the far field to the near field was an increase in SRH01 with tornadic supercells. Acceleration of low-level flow toward the updraft by dynamically induced low pressure perturbations accompanying the mesocyclone is the most intuitive mechanism for enlargement of near-field hodographs and SRH01. Despite some case-to-case inconsistency in observing this effect, it is statistically significant. Such enlargement is not found in the nontornadic set, possibly a reflection of less intense or poorly organized low-level mesocyclones.

Steep low-level lapse rates were often observed in the inflow of both tornadic and nontornadic supercells. In the far-field environments, the boundary layers were deeper/warmer in the tornadic soundings. Some of this difference could be related to the tendency for the far-field tornadic soundings to be taken earlier in the day near peak heating. However, the higher dewpoints through the lowest 3 km are noteworthy. Although the moisture increases substantially in the near field of the nontornadic soundings, it remains greater for the tornadic soundings. The moist layer may be slightly deeper,
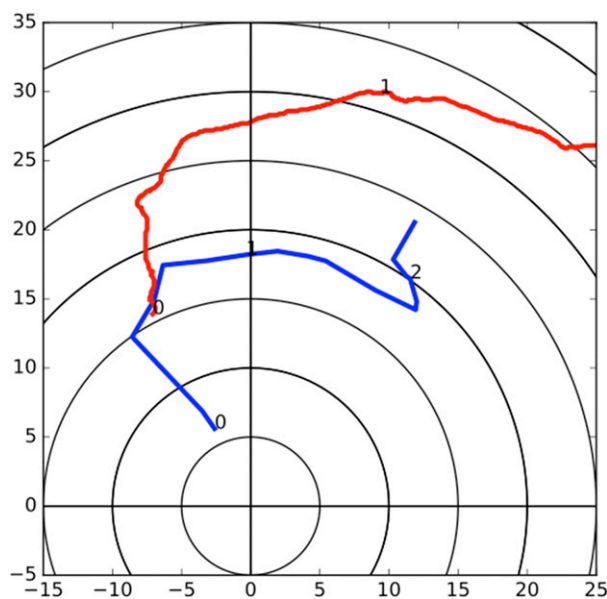
FIG. 9. Hodographs to 3 km AGL for a 2300 UTC MPEX sounding (red) in the near inflow of the 31 May 2013 El Reno supercell and the 0000 UTC KOUN sounding (blue) that qualifies as far inflow.

too, though elevation differences complicate this comparison. This suggests that the low-level updrafts for the tornadic soundings could be experiencing less dilution from relatively dry air, assisting tornadogenesis by increasing buoyancy-driven updraft acceleration and associated low-level vortex stretching.

The steep near-ground lapse rates observed in the far field tended to persist into the near inflow. Evidence of consistent cooling in the near inflow of tornadic storms was lacking; cooling was absent about as often as it was present, and even a slight increase in potential temperature in the near field of tornadic supercells was sometimes noted. If in fact maintenance of low near-ground static stability is characteristic of tornadic supercells, it could relate to tornado production (presumably through enhanced low-level stretching of the updraft).

The first step of any future work in this area should be to collect a broader sample of simultaneous inflow sounding pairs, if possible. The current set of tornadic pairs is centered earlier in the day than the nontornadic pairs, and the dataset consists only of springtime Great Plains environments with moderate to extreme instability. A larger number of soundings might also allow interpolation to truly vertical near-field profiles as in P14, as opposed to observed soundings that drift with the flow. Denser spatiotemporal sampling of individual storms is also desirable for describing the spatial extent of storm-induced changes and their dependence on the time elapsed since storm initiation. This would require

use of additional mobile sounding vehicles, unmanned aerial systems, or both. Furthermore, denser sampling could clarify the ambient (nonstorm induced) spatiotemporal variability of all parameters on the scales in question. Further research might attempt to connect near-inflow low-level lapse rates to low-level flow enhancement more definitively, with both observations and numerical modeling.

APPENDIX

Consideration of RAP Background Profiles

One prospective way to maximize the sample size of near-/far-field simultaneous pairs was to use Rapid Refresh (RAP) model (Benjamin et al. 2016) analysis "soundings" as the background or far-field profiles. Profiles from its predecessor, the Rapid Update Cycle (Benjamin et al. 2004), were often used in studies that assessed the effects of the environment on storms (e.g., Thompson et al. 2003). To determine whether RAP profiles could be used effectively in this way, it was necessary to test them for biases in similar scenarios—warm-season, mostly diurnal, convectively unstable Great Plains environments.

For comparison to RAP soundings, 102 environmental soundings (no deep convection within 80 km) from MPEX were selected. Some were from days where storms were expected but did not form nearby. Others were launched before convective initiation. Still others were in inflow, but were more than 80 km away from any robust storm and were assumed to remain unaffected (Potvin et al. 2010). RAP analyses were obtained at the nearest hour for these cases, and vertical profiles were

created at the grid point nearest the sounding release site. To avoid making assumptions about the unknown distribution of RAP errors, bootstrapping (e.g., Wilks 1995)—rather than a *t* test or some similar method—was chosen for statistical assessment of potential RAP biases. Confidence intervals for RAP biases in several relevant variables were bootstrapped with 5000 replicates.

The only statistically significant differences between the radiosonde and RAP soundings were all directly related to a known daytime warm and dry bias near the surface in the RAP analyses (Weygandt et al. 2015). With 95% confidence, the RAP warm bias in surface temperature was 1.17–2.09 K and the dry bias in surface dewpoint temperature was 0.83–2.50 K. It will be shown that these errors are similar in magnitude to typical storm-induced changes to supercell inflow. These errors were present during spring 2016 MiniMPEX operations as well, since the implementation of the RAP that is expected to reduce these biases became operational in October 2016. This precludes using RAP profiles as a base state for comparison to observed near-storm soundings. However, successfully replicating the known warm and dry bias of the RAP validates the use of radiosonde observations to investigate small changes in the near-storm boundary layer.

REFERENCES

Barnes, S. L., 1978: Oklahoma thunderstorms on 29-30 April 1970. Part I: Morphology of a tornadic storm. *Mon. Wea. Rev.*, **106**, 673–684, https://doi.org/10.1175/1520-0493(1978)106<0673:OTOAPI>2.0.CO;2.

Beebe, R. G., 1956: Tornado composite charts. *Mon. Wea. Rev.*, **84**, 127–142, https://doi.org/10.1175/1520-0493(1956)084<0127:TCC>2.0.CO;2.

Benjamin, S. G., and Coauthors, 2004: An hourly assimilation-forecast cycle: The RUC. *Mon. Wea. Rev.*, **132**, 495–518, https://doi.org/10.1175/1520-0493(2004)132<0495:AHACTR>2.0.CO;2.

——, and Coauthors, 2016: A North American hourly assimilation and model forecast cycle: The Rapid Refresh. *Mon. Wea. Rev.*, **144**, 1669–1694, https://doi.org/10.1175/MWR-D-15-0242.1.

Brooks, H. E., C. A. Doswell III, and J. Cooper, 1994: On the environments of tornadic and nontornadic mesocyclones. *Wea. Forecasting*, **9**, 606–618, https://doi.org/10.1175/1520-0434(1994)009<0606:OTEOTA>2.0.CO;2.

Bunkers, M. J., B. A. Klimowski, J. W. Zeitler, R. L. Thompson, and M. L. Weisman, 2000: Predicting supercell motion using a new hodograph technique. *Wea. Forecasting*, **15**, 61–79, https://doi.org/10.1175/1520-0434(2000)015<0061:PSMUAN>2.0.CO;2.

Coffer, B. E., and M. D. Parker, 2017: Simulated supercells in non-tornadic and tornadic VORTEX2 environments. *Mon. Wea. Rev.*, **145**, 149–180, https://doi.org/10.1175/MWR-D-16-0226.1.

——, ——, J. M. L. Dahl, L. J. Wicker, and A. J. Clark, 2017: Volatility of tornadogenesis: An ensemble of simulated nontornadic and tornadic supercells in VORTEX2 environments. *Mon. Wea. Rev.*, **145**, 4605–4625, https://doi.org/10.1175/MWR-D-17-0152.1.

Craven, J. P., and H. E. Brooks, 2004: Baseline climatology of sounding derived parameters associated with deep, moist convection. *Natl. Wea. Dig.*, **28**, 13–24.

Dessens, M., 1960: Severe hailstorms are associated with very strong winds between 6,000 and 12,000 meters. *Physics of Precipitation: Proceedings of the Cloud Physics Conference*, Geophys. Monogr., Vol. 5, Amer. Geophys. Union, 333–338, https://doi.org/10.1029/GM005p0333.

Esterheld, J. M., and D. J. Giuliano, 2008: Discriminating between tornadic and non-tornadic supercells: A new hodograph technique. *Electron. J. Severe Storms Meteor.*, **3** (2), http://www.ejssm.org/ojs/index.php/ejssm/article/viewArticle/33.

Fankhauser, J. C., 1971: Thunderstorm–environment interactions determined from aircraft and radar observations. *Mon. Wea. Rev.*, **99**, 171–192, https://doi.org/10.1175/1520-0493(1971)099<0171:TIDFAA>2.3.CO;2.

Gilmore, M. S., and L. J. Wicker, 1998: The influence of mid-tropospheric dryness on supercell morphology and evolution. *Mon. Wea. Rev.*, **126**, 943–958, https://doi.org/10.1175/1520-0493(1998)126<0943:TIOMDO>2.0.CO;2.

Grant, L. D., and S. C. van den Heever, 2014: Microphysical and dynamical characteristics of low-precipitation and classic supercells. *J. Atmos. Sci.*, **71**, 2604–2624, https://doi.org/10.1175/JAS-D-13-0261.1.

Hart, J. A., and W. Korotky, 1991: The SHARP workstation v1.50 user's guide. National Weather Service, NOAA, U.S. Department of Commerce, 30 pp. [Available from NWS Eastern Region Headquarters, 630 Johnson Ave., Bohemia, NY 11716.]

Houston, A. L., 2017: The possible role of density current dynamics in the generation of low-level vertical vorticity in supercells. *J. Atmos. Sci.*, **74**, 3191–3208, https://doi.org/10.1175/JAS-D-16-0227.1.

James, R. P., and P. M. Markowski, 2010: A numerical investigation of the effects of dry air aloft on deep convection. *Mon. Wea. Rev.*, **138**, 140–161, https://doi.org/10.1175/2009MWR3018.1.

Kerr, C. A., D. J. Stensrud, and X. Wang, 2017: Verification of convection-allowing model ensemble analyses of near-storm environments using MPEX upsonde observations. *Mon. Wea. Rev.*, **145**, 857–875, https://doi.org/10.1175/MWR-D-16-0287.1.

Lilly, D. K., 1986: The structure, energetics, and propagation of rotating convective storms. Part I: Energy exchange with the mean flow. *J. Atmos. Sci.*, **43**, 113–125, https://doi.org/10.1175/1520-0469(1986)043<0113:TSEAPO>2.0.CO;2.

Loehrer, S. M., S. F. Williams, and J. A. Moore, 1998: Results from UCAR/JOSS quality control of atmospheric soundings from field projects. Preprints, *10th Symp. on Meteorological Observations and Instrumentation,* Phoenix, AZ, Amer. Meteor. Soc., 1–6.

Markowski, P. M., and Y. P. Richardson, 2014: The influence of environmental low-level shear and cold pools on tornadogenesis: Insights from idealized simulations. *J. Atmos. Sci.*, **71**, 243–275, https://doi.org/10.1175/JAS-D-13-0159.1.

——, J. M. Straka, E. N. Rasmussen, and D. O. Blanchard, 1998a: Variability of storm-relative helicity during VORTEX. *Mon. Wea. Rev.*, **126**, 2959–2971, https://doi.org/10.1175/1520-0493(1998)126<2959:VOSRHD>2.0.CO;2.

——, E. N. Rasmussen, J. M. Straka, and D. C. Dowell, 1998b: Observations of low-level baroclinity generated by anvil shadows. *Mon. Wea. Rev.*, **126**, 2942–2958, https://doi.org/10.1175/1520-0493(1998)126<2942:OOLLBG>2.0.CO;2.

——, C. Hannon, J. Frame, E. Lancaster, A. Pietrycha, R. Edwards, and R. L. Thompson, 2003: Characteristics of vertical wind profiles near supercells obtained from the Rapid Update Cycle. *Wea. Forecasting*, **18**, 1262–1272, https://doi.org/10.1175/1520-0434(2003)018<1262:COVWPN>2.0.CO;2.

McCaul, E. W., and M. L. Weisman, 2001: The sensitivity of simulated supercell structure and intensity to variations in the shapes of

buoyancy and shear profiles. *Mon. Wea. Rev.*, **129**, 664–687, https://doi.org/10.1175/1520-0493(2001)129<0664:TSOSSS>2.0.CO;2.

Miller, D. J., 2006: Observations of low level thermodynamic and wind shear profiles on significant tornado days. *23rd Conf. on Severe Local Storms*, St. Louis, MO, Amer. Meteor. Soc., 1206–1223.

Nowotarski, C. J., and P. M. Markowski, 2016: Modifications to the near-storm environment induced by simulated supercell thunderstorms. *Mon. Wea. Rev.*, **144**, 273–293, https://doi.org/10.1175/MWR-D-15-0247.1.

Parker, M. D., 2014: Composite VORTEX2 supercell environments from near-storm soundings. *Mon. Wea. Rev.*, **142**, 508–529, https://doi.org/10.1175/MWR-D-13-00167.1.

Potvin, C. K., K. L. Elmore, and S. J. Weiss, 2010: Assessing the impacts of proximity sounding criteria on the climatology of significant tornado environments. *Wea. Forecasting*, **25**, 921–930, https://doi.org/10.1175/2010WAF2222368.1.

Rasmussen, E. N., 2003: Refined supercell and tornado forecast parameters. *Wea. Forecasting*, **18**, 530–535, https://doi.org/10.1175/1520-0434(2003)18<530:RSATFP>2.0.CO;2.

——, and D. O. Blanchard, 1998: A baseline climatology of sounding-derived supercell and tornado forecast parameters. *Wea. Forecasting*, **13**, 1148–1164, https://doi.org/10.1175/1520-0434(1998)013<1148:ABCOSD>2.0.CO;2.

Straka, J. M., E. N. Rasmussen, and S. E. Fredrickson, 1996: A mobile mesonet for finescale meteorological observations. *J. Atmos. Oceanic Technol.*, **13**, 921–936, https://doi.org/10.1175/1520-0426(1996)013<0921:AMMFFM>2.0.CO;2.

Thompson, R. L., and R. Edwards, 2000: An overview of environmental conditions and forecast implications of the 3 May 1999 tornado outbreak. *Wea. Forecasting*, **15**, 682–699, https://doi.org/10.1175/1520-0434(2000)015<0682:AOOECA>2.0.CO;2.

——, ——, and J. A. Hart, 2002: Evaluation and interpretation of the supercell composite and significant tornado parameters at the Storm Prediction Center. Preprints, *21st Conf. on Severe Local Storms,* San Antonio, TX, Amer. Meteor. Soc., J11–J14.

——, ——, ——, K. L. Elmore, and P. Markowski, 2003: Close proximity soundings within supercell environments obtained from the Rapid Update Cycle. *Wea. Forecasting*, **18**, 1243–1261, https://doi.org/10.1175/1520-0434(2003)018<1243:CPSWSE>2.0.CO;2.

——, B. T. Smith, J. S. Grams, A. R. Dean, and C. Broyles, 2012: Convective modes for significant severe thunderstorms in the contiguous United States. Part II: Supercell and QLCS tornado environments. *Wea. Forecasting*, **27**, 1136–1154, https://doi.org/10.1175/WAF-D-11-00116.1.

Trapp, R. J., D. J. Stensrud, M. C. Coniglio, R. S. Schumacher, M. E. Baldwin, S. Waugh, and D. T. Conlee, 2016: Mobile radiosonde deployments during the Mesoscale Predictability Experiment (MPEX): Rapid and adaptive sampling of upscale convective feedbacks. *Bull. Amer. Meteor. Soc.*, **97**, 329–336, https://doi.org/10.1175/BAMS-D-14-00258.1.

UCAR/NCAR/CISL/TDD, 2014: NCAR Command Language (version 6.2.1) [Software]. UCAR/NCAR/CISL/TDD, Boulder, CO, https://doi.org/10.5065/D6WD3XH5.

Weisman, M. L., and J. B. Klemp, 1982: The dependence of numerically simulated convective storms on vertical wind shear and buoyancy. *Mon. Wea. Rev.*, **110**, 504–520, https://doi.org/10.1175/1520-0493(1982)110<0504:TDONSC>2.0.CO;2.

——, and ——, 1984: The structure and classification of numerically simulated convective storms in directionally varying wind shears. *Mon. Wea. Rev.*, **112**, 2479–2498, https://doi.org/10.1175/1520-0493(1984)112<2479:TSACON>2.0.CO;2.

——, and Coauthors, 2015: The Mesoscale Predictability Experiment (MPEX). *Bull. Amer. Meteor. Soc.*, **96**, 2127–2149, https://doi.org/10.1175/BAMS-D-13-00281.1.

Weygandt, S. S., and Coauthors, 2015: Rapid Refresh: Version 2 upgrade at NCEP and work toward version 3 and the North American Rapid Refresh Ensemble (NARRE). *Fifth Conf. on Transition from Research to Operations*, Phoenix, AZ, Amer. Meteor. Soc., 4.1, https://ams.confex.com/ams/95Annual/webprogram/Paper267898.html.

Whiting, R. M., and R. E. Bailey, 1957: Some meteorological relationships in the prediction of tornadoes. *Mon. Wea. Rev.*, **85**, 141–150, https://doi.org/10.1175/1520-0493(1957)085<0141:SMRITP>2.0.CO;2.

Wicker, L. J., 1996: The role of near surface wind shear on low-level mesocyclone generation and tornadoes. Preprints, *18th Conf. on Severe Local Storms*, San Francisco, CA, Amer. Meteor. Soc., 115–119.

Wilks, D. S., 1995: *Statistical Methods in the Atmospheric Sciences: An Introduction.* Academic Press, 464 pp.

Williams, R. J., 1976: Surface parameters associated with tornadoes. *Mon. Wea. Rev.*, **104**, 540–545, https://doi.org/10.1175/1520-0493(1976)104<0540:SPAWT>2.0.CO;2.

Wurman, J., D. Dowell, Y. Richardson, P. Markowski, E. Rasmussen, D. Burgess, L. Wicker, and H. B. Bluestein, 2012: The second Verification of the Origins of Rotation in Tornadoes Experiment: VORTEX2. *Bull. Amer. Meteor. Soc.*, **93**, 1147–1170, https://doi.org/10.1175/BAMS-D-11-00010.1.

Yurchak, B. S., 2013: An assessment of radiosonde launch conditions affected by the surface wind. *Russ. Meteor. Hydrol.*, **38**, 159–167, https://doi.org/10.3103/S1068373913030035.

Ziegler, C. L., and E. N. Rasmussen, 1998: The initiation of moist convection at the dryline: Forecasting issues from a case study perspective. *Wea. Forecasting*, **13**, 1106–1131, https://doi.org/10.1175/1520-0434(1998)013<1106:TIOMCA>2.0.CO;2.

——, E. R. Mansell, J. M. Straka, D. R. MacGorman, and D. W. Burgess, 2010: The impact of spatial variations of low-level stability on the life cycle of a simulated supercell storm. *Mon. Wea. Rev.*, **138**, 1738–1766, https://doi.org/10.1175/2009MWR3010.1.